J. Fluid Mech. (2005), *vol.* 530, *pp.* 305–325.
doi:10.1017/S002211200500371X Printed in the United Kingdom

Quasi-geostrophic vortices in compressible atmospheres

By RICHARD K. SCOTT† AND DAVID G. DRITSCHEL
Mathematical Institute, University of St Andrews, North Haugh, St Andrews KY16 9SS, UK

(Received 16 March 2004 and in revised form 14 December 2004)

This paper considers the effect of an exponential variation in the background density field (as exists in compressible atmospheres) on the structure and dynamics of the quasi-geostrophic system, and compares the results with the corresponding Boussinesq limit in which background density variations are assumed small. The behaviour of the compressible system is understood via a closed-form analytic expression for the Green's function of the inversion operator relating potential vorticity and streamfunction. This expression makes explicit the anisotropy of the Green's function, inherited from the density profile, which has a slow, algebraic decay directly above the source and an exponential decay in all other directions. An immediate consequence for finite-volume vortices is a differential rotation of upper and lower levels that results in counterintuitive behaviour during the nonlinear evolution of ellipsoidal vortices, in which vortex destruction is confined to the lower vortex and wave activity is seen to propagate downwards. This is in contrast to the Boussinesq limit, which exhibits symmetric destruction of the upper and lower vortex, and in contrast to naive expectations based on a consideration of the mass distribution alone, which would lead to greater destruction of the upper vortex. Finally, the presence of a horizontal lower boundary introduces a strong barotropic component that is absent in the unbounded case (the presence of an upper boundary has almost no effect). The lower boundary also alters the differential rotation in the lower vortex with important consequences for the nonlinear evolution: for very small separation between the lower boundary and the vortex, the differential rotation is reversed leading to strong deformations of the middle vortex; for a critical separation, the vortex is stabilized by the reduction of the differential rotation, and remains coherent over remarkably long times.

1. Introduction

The evolution of coherent vortical structures in rotating stratified fluid has long been recognized as a central theme in typical geophysical flows. This motion constitutes an approximate slow-manifold to which the low-frequency balanced motion is restricted by constraints imposed by the rotation and stratification. On this manifold, the flow is characterized by a single scalar quantity, the potential vorticity, which is materially conserved and which, under suitable balance conditions that eliminate high-frequency gravity wave motions, can be exactly inverted to obtain all other variables of the flow. By defining the length scales over which a given potential vorticity structure has

† Present address: Northwest Research Associates, PO Box 3027, Bellevue, WA 98009-3027, USA.

an influence on the external flow field, the form of the inversion operator essentially characterizes the balanced system.

Because of the dominant hydrostatic and geostrophic balances, fluid particles in typical geophysical flows are constrained to lie on quasi-horizontal surfaces and the motion is layerwise two-dimensional. For this reason, the flow is often modelled as two-dimensional barotropic flow, in which the potential vorticity reduces to the vertical component of the ordinary vorticity. However, the inversion relation relating the potential vorticity (PV) and streamfunction in the two-dimensional barotropic model has very different decay properties from that of any three-dimensional system. Specifically, the two-dimensional barotropic inversion operator is the inverse of the two-dimensional Laplacian, whose Green's function has a logarithmic dependence on the two-dimensional distance.

The simplest (non-trivial) three-dimensional model of rotating stratified flow is the Boussinesq form of the three-dimensional quasi-geostrophic equations, obtained from the standard quasi-geostrophic equations (defined below) by assuming that density variations are a small perturbation to a uniform background density profile. This assumption is appropriate for fluid motion in the oceans. In that case, using a suitably scaled vertical coordinate, the inversion operator is the inverse of the usual three-dimensional Laplacian, and the Green's function decays as the inverse of the three-dimensional distance.

In the atmosphere, because the vertical density profile is exponentially decreasing with height, the Boussinesq approximation of constant background density is a poor approximation to flows spanning more than a density scale height, H. For such flows, it is appropriate to retain the exponential dependence of background density, $\rho = \rho_s \exp -z/H$, leading to what we refer to here as the compressible quasi-geostrophic system. If the vertical domain is bounded, it is possible to decompose the equations into vertical modes, each mode possessing a (horizontal) two-dimensional equivalent barotropic structure (Waugh & Dritschel 1999). The inversion operators for these modes are of Helmholtz form, and the Green's function for each mode decays exponentially in the horizontal direction with a length scale given by the Rossby radius of deformation, L_R, the length scale on which gravitational and Coriolis forces balance (Waugh & Dritschel 1991).

In this paper we show how the Green's function for the compressible quasi-geostrophic equations in an unbounded vertical domain can be constructed analytically using a non-standard separation of variables involving a vertical coordinate and a three-dimensional radial coordinate. This analytic form shows explicitly that the decay is anisotropic, with exponential decay in every direction except vertically above the source, where the decay is algebraic as in the Boussinesq limit. In particular, the vertical decay is exponential below and algebraic above. An important consequence of this anisotropy is that upper and lower regions of a finite-volume of uniform potential vorticity have different rotation rates, the upper part rotating faster because the induced circulation of the vortex core decays more slowly above than below.

The full implications of this anisotropy for finite-volume vortices and their nonlinear evolution are further investigated using high-resolution numerical modelling. Anisotropy in the atmosphere and its importance for vertical wave propagation are well known. One the one hand, the exponential decrease in density with height means that wave amplitudes (as measured by particle displacements) will increase for upward propagating waves and decrease for downward propagating waves. For a spectrum of upward and downward propagating waves, wave breaking will therefore

tend to occur at upper levels. On the other hand, as is shown below, the differential rotation associated with the Green's function means that general disturbances more readily lead to downward propagation than to upward. For the potential vorticity distributions studied here, the latter effect is dominant and almost all wave breaking is confined to lower vortex levels.

Finally, the effect of upper and lower boundaries on this isotropy is considered. It turns out that when the lower boundary is about one scale-height distant from the bottom of the vortex there is an almost exact cancellation between the tendency for downward propagation on the free space vortex and the barotropization of the Green's function response by the lower boundary. This distance corresponds roughly to the distance between the ground and the bottom of the winter stratospheric polar vortex.

2. Green's function for the compressible case

The quasi-geostrophic system is the simplest model of rotating stratified flow. It is derived from the primitive equations (e.g. Pedlosky 1987) by an asymptotic expansion in Rossby number, Ro, the ratio of the normal component of the relative vorticity ζ to the normal component of the planetary vorticity $f = 2\Omega \sin\phi$, and the Froude number Fr, the ratio of the horizontal velocity U to the gravity wave speed associated with the stratification $c = NH$. Here, Ω is the planetary rotation rate, ϕ is latitude, N is the buoyancy frequency, and H is a vertical length scale and is assumed to be much smaller than the horizontal length scale L. Taking $Fr^2 \ll Ro \ll 1$ results in the usual quasi-geostrophic system applicable to midlatitude planetary scale motions.

In dimensional variables this system takes the form:

$$\frac{\mathrm{D}q}{\mathrm{D}t} \equiv \frac{\partial q}{\partial t} + \boldsymbol{u} \cdot \nabla q = 0, \tag{2.1a}$$

$$\nabla_h^2 \psi + \frac{1}{\rho}\frac{\partial}{\partial z}\left(\rho \frac{f^2}{N^2}\frac{\partial \psi}{\partial z}\right) = q, \tag{2.1b}$$

$$(u, v) = \left(-\frac{\partial \psi}{\partial y}, \frac{\partial \psi}{\partial x}\right), \tag{2.1c}$$

where, $q(x, y, z, t)$ is the potential vorticity (PV), ψ is the geostrophic streamfunction, $\boldsymbol{u} = (u, v)$ is the horizontal geostrophic velocity, ρ is the background density, ∇_h^2 is the horizontal Laplacian, x and y are horizontal coordinates and $z \propto -H \log p$ is an appropriate log-pressure vertical coordinate.

For simplicity, we make the further assumption that f and N are constant, which allows the vertical coordinate z to be rescaled by f/N. We also assume that the density decreases exponentially with height as $\rho = \rho_s \exp(-z/H)$, where ρ_s is a surface reference density, which is a natural approximation in the atmospheric context. Further, scaling horizontal and vertical coordinates by $L = NH/f$ and H, respectively, allows (2.1b) to be written as

$$\nabla^2 \psi - \frac{\partial \psi}{\partial z} = q, \tag{2.2}$$

where ∇^2 is the usual three-dimensional Laplacian.

Under the Boussinesq approximation, in which the background density is approximately constant, (2.1b) simplifies further by the elimination of the term $\partial\psi/\partial z$. The

effect of compressibility, therefore, is the retention of an anisotropy in the inversion relation between ψ and q.

Separation of variables is possible using R and z as independent coordinates, where $R = \sqrt{x^2 + y^2 + (z - z')^2}$ is a full three-dimensional radial coordinate from a source point located at $(0, 0, z')$, without any loss of generality. The Green's function for (2.2) satisfies the equation

$$\nabla^2 G_\infty - \frac{\partial G_\infty}{\partial z} = \delta(r, z - z'), \tag{2.3}$$

where $r = \sqrt{x^2 + y^2}$ is a horizontal radial coordinate. Posing a solution of the form $G_\infty(R, z; z') = (\rho'/\rho)^{1/2} F(R)$, it can be shown directly that G_∞ has the form

$$G_\infty(R, z; z') = -\frac{1}{4\pi} \left(\frac{\rho'}{\rho}\right)^{1/2} \frac{\mathrm{e}^{-R/2}}{R}, \tag{2.4}$$

where we have used the shorthand notation for the density $\rho = \mathrm{e}^{-z}$ and $\rho' = \mathrm{e}^{-z'}$. Note that the same Green's function structure arises in the context of the advection–diffusion equation with uniform flow, whose operator also takes the form (2.2) (see, e.g. Morton 1996).

Directly above and below the source, i.e. along the vertical line $r = 0$, G_∞ reduces to

$$G_\infty(r = 0) = -\frac{1}{4\pi|z - z'|} \begin{cases} 1 & \text{for } z > z', \\ \rho'/\rho & \text{for } z < z'. \end{cases} \tag{2.5}$$

The anisotropy introduced by the compressibility term in (2.2) is now apparent: above the source point z', the Green's function decays algebraically like $1/R$, similar to the Boussinesq limit, whereas below the source the decay is exponential, with a decay scale of one (H in dimensional units). Note that locally, i.e. for $R \ll 1$, $G_\infty \sim 1/4\pi R$, which is the form taken by the Boussinesq Green's function. The structure of G_∞ is shown by figure 1(b). Again, the anisotropy introduced by the compressibility is evident.

We next compare the properties of the free-space Green's function G_∞ with the Green's function G_D obtained by Waugh & Dritschel (1999, their equation 5b rescaled by a factor of $\rho(z')$ for consistency) in a vertically bounded domain of depth D, with $\psi_z =$ at $z = 0$ and $z = D$. We note in passing that it is impossible to construct G_D from G_∞ using the method of images because the anisotropic term in (2.2) breaks the necessary symmetry in the vertical coordinate. Figure 1(a) shows G_D in a domain of depth $D = 12$, whose boundaries coincide with the upper and lower boundaries of the figures, for various locations of the source point z'. When z' is well away from either boundary, the agreement between G_∞ and G_D is very good: figure 1(c) shows the difference $G_D - G_\infty$. In other words, boundaries have a very weak effect if they are far enough away. When z' is located near the upper boundary, the structure of G_∞ is also very similar to G_D, with only the magnitude being increased by the presence of the upper boundary.

On the other hand, it is immediately clear from the lower panels in figure 1 that the presence of the lower boundary greatly influences the bounded Green's function. As the source point z' approaches the lower boundary, G_D becomes increasingly dominated by a strong barotropic component, associated with the zeroth mode in the vertical decomposition. That mode has a horizontal dependence of the form $\log r$, (cf. the two-dimensional barotropic model), in contrast to the exponential horizontal decay of all higher modes (cf. the two-dimensional equivalent barotropic model).

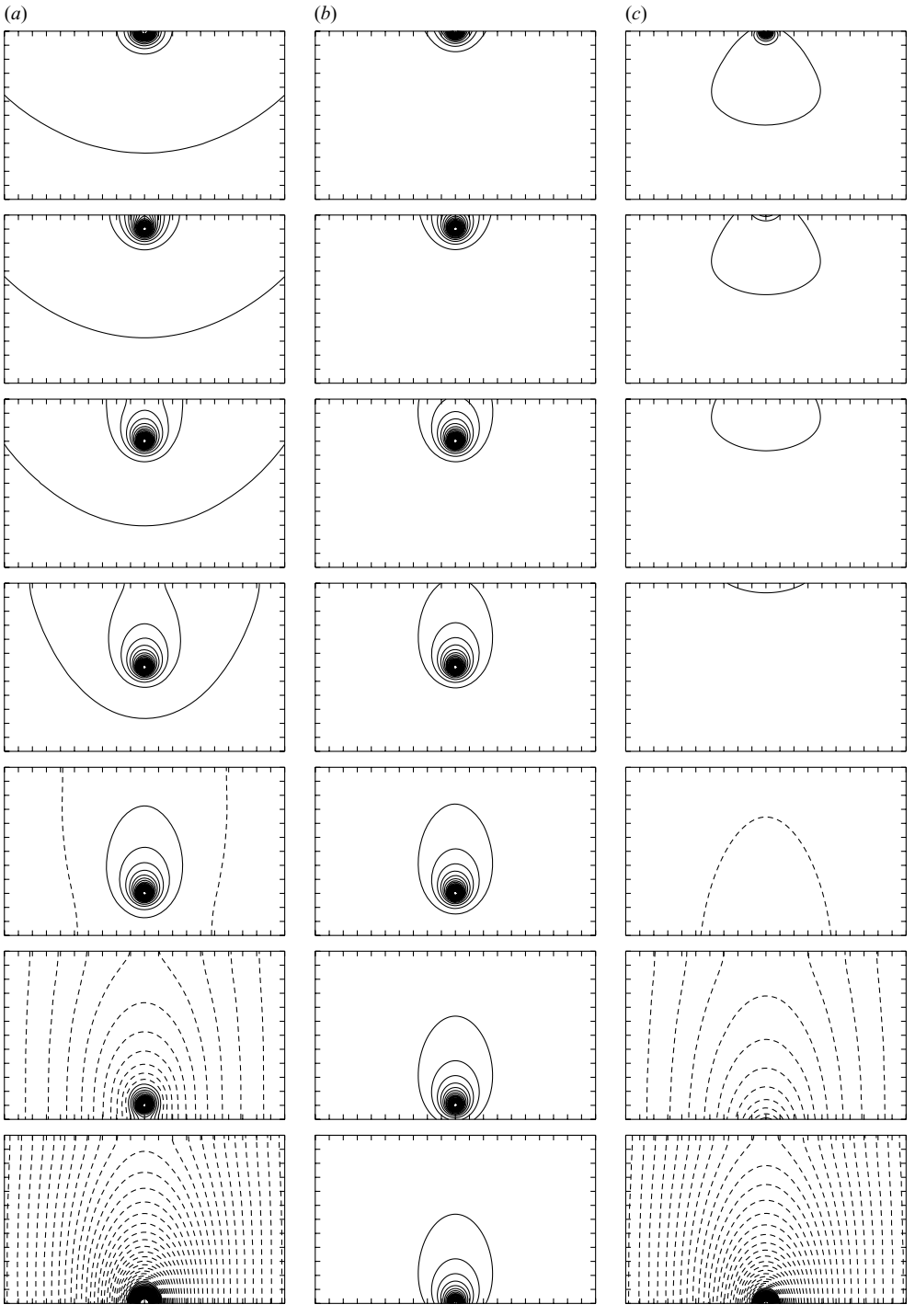

FIGURE 1. (*a*) Bounded and (*b*) free-space Green's functions, G_D and G_∞, respectively, and (*c*) their difference, $G_D - G_\infty$, for the compressible quasi-geostrophic inversion relation (2.3). For G_D, the source is located at $z_0 = 12, 11, 9, 6, 3, 1, 0$ in units of scale-height H, and the vertical domain is 12. Tickmarks are at unit intervals on the horizontal (r) and vertical (z) axes. Negative contours are dashed.

It becomes large when z' lies within one or two density scale heights of the lower boundary.

3. Finite vortices

Having described the Green's function for the inversion problem, we are in a position to understand the consequences of density anisotropy for the properties of finite-volume vortices. In this section, we consider the simplest configuration, that of a spherical patch of uniform potential vorticity. We note that, for spheres of radius much smaller than the density scale height, the Boussinesq limit is recovered (for the flow field within and close to the vortex).

The velocity field induced by an arbitrary three-dimensional patch of uniform PV is given by (see Dritschel 1989)

$$\boldsymbol{u}(\boldsymbol{x}, z) = -q \int_0^D \mathrm{d}z' \oint_{\Gamma(z')} G_\infty(\boldsymbol{x}, z; \boldsymbol{x}', z')\, \mathrm{d}\{x', y'\}, \tag{3.1}$$

where $\boldsymbol{x} = (x, y)$ is the horizontal position, and where the horizontal integral is taken around a contour enclosing the horizontal cross-section of the patch at height z'. In the examples presented in this section, the velocity field was calculated numerically using the contour dynamics algorithm described below, using 480 horizontal layers spanning the depth of the vortex patch. The algorithm essentially computes (3.1) in each horizontal layer and sums the induced velocity fields. See § 4 below for further details.

Because G_∞ decays more slowly above the vortex than below, we expect the rotation rate of the upper vortex to be greater than that of the lower vortex: PV at the vortex centre induces a stronger circulation above than below. This is illustrated in figure 2, which shows the velocity (upper panels) and angular velocity, or rotation rate (lower panels) for spherical PV patches of varying depths $D = 1/4, 2,$ and 16. As expected, for $D = 1/4$ the vortex rotates approximately as a solid body, as it would in the absence of compressibility. Similarly, the exterior velocity and angular velocity fields are almost symmetric in z. For larger D, the effects of the compressibility become apparent: in particular, the angular velocity within the vortex develops a strong vertical dependence, increasing with z and with a maximum at the top of the vortex. Outside the vortex, both fields show much weaker decay above the vortex, consistent with the properties of the Green's function.

For large D, the angular velocity ω along the vortex axis has a clear maximum at $z = D$, a consequence of the weakest decay of G_D being directly above the source point. In figure 3(a), we plot ω along the vortex axis as a function of height, z/D, within the vortex for vortex depths $D = 1/16, 1/8, \ldots, 16, 32$. The profile for $D = 1/16$ is almost exactly constant with $\omega \approx 2$. As D increases, the average rotation rate decreases, in contrast to the Boussinesq case where $\omega = 2$ regardless of vortex size. Again, this is a result of the shorter-range nature of G_∞. At the top of the vortex, however, where the influence of the lower vortex decays more slowly, ω actually increases beyond the Boussinesq value with increasing D, reaching a maximum for $D \approx 4$. This can be seen from the solid line in figure 3(b) which shows ω at the top of the vortex. As will be seen below, this differential rotation, which maximizes at $D \approx 8$, plays an important role in the nonlinear evolution of an ellipsoidal disturbance on a spherical patch.

Finally, from figure 2, it can be seen that the velocity field has a maximum that moves upward off the horizontal plane of symmetry as D increases. The value of the

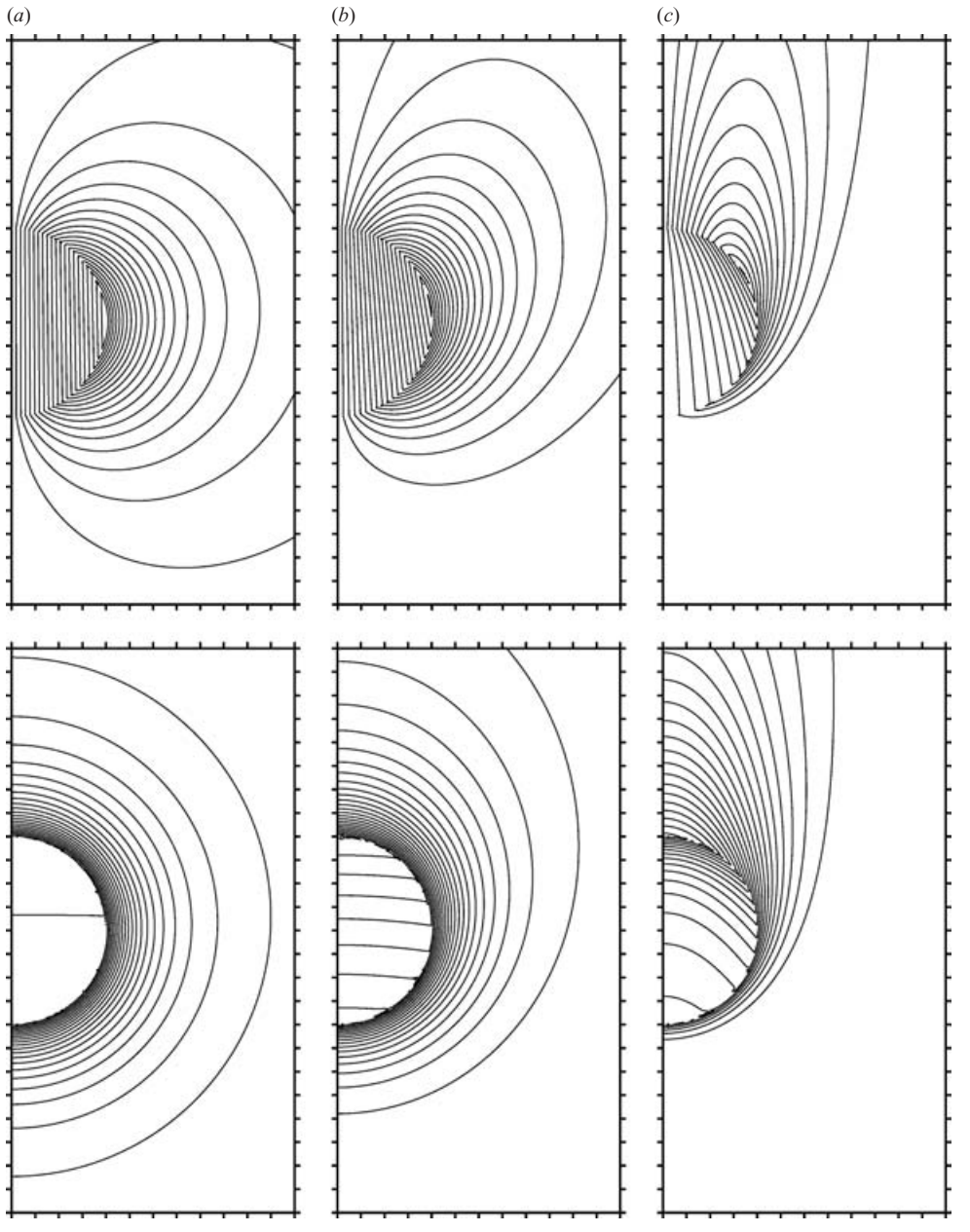

FIGURE 2. Azimuthal velocity (upper panels) and angular velocity (lower panels) corresponding to spherical patches of uniform PV of diameters (*a*) $D = 1/4$, (*b*) $D = 2$ and (*c*) $D = 16$ in the unbounded compressible case. Contour interval is $D/20$ for the velocity and 0.1 for the angular velocity; tickmarks on horizontal (r) and vertical (z) axes are every $D/8$. Calculation is made using $n_\ell = 640$ vertical layers (see § 4).

velocity maximum, divided by the vortex radius $D/2$, is plotted in figure 3*b* (dotted line) and shows a steady decrease with increasing D, again a result of the short range nature of G_∞ and the fact that the velocity maximum is located away from the vertical axis.

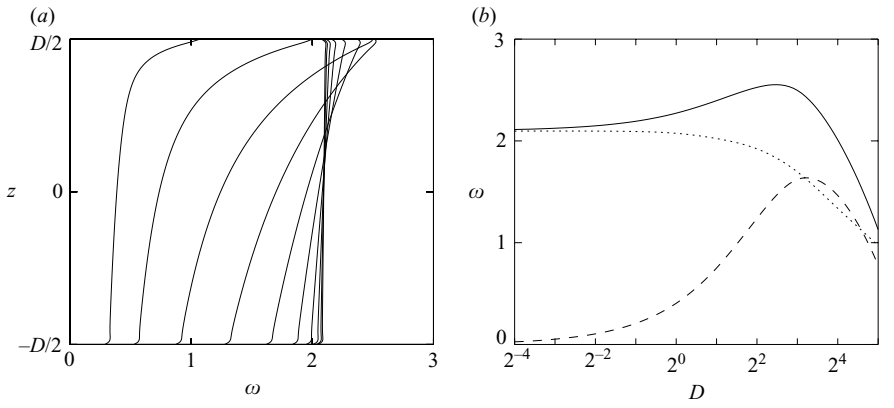

FIGURE 3. (*a*) Angular velocity $\omega(z)$ along the vertical axis of rotation for spherical vortices of diameters $D = 1/16, 1/8, \ldots, 16, 32$ (D decreasing left to right, with $D = 1/16$ approximately vertical); (*b*) —, maximum angular velocity ω_{max}; . . . , maximum azimuthal velocity divided by vortex radius $u_{max}/(D/2)$; - - -, differential angular velocity $\omega(D/2) - \omega(-D/2)$ as a function of vortex size D.

4. Numerical methods

Two related numerical methods have been used to simulate the nonlinear evolution of vortices having a variety of initial shapes and sizes. Both methods explicitly advect material PV contours, but differ in the way they compute the velocity field $\boldsymbol{u}$ from these contours. The first method, contour dynamics or contour surgery (CS), solves (3.1) directly, by vertically discretizing the flow into n_ℓ layers spanning the vortex. As there is no vertical advection, the vertical extent of the PV distribution does not change. The velocity $\boldsymbol{u}$ is evaluated directly on the contours $\boldsymbol{x} \in \Gamma(z)$, for z in the middle of each layer. The contours themselves are discretized into a variable number of points (adjusted dynamically to maintain adequate resolution). The details differ little from those described in Dritschel (2002) for the Boussinesq case ($G_\infty = -1/4\pi R$), apart from the way in which the vertical integration is performed in (3.1). In the Boussinesq case, the integration is done explicitly owing to the simple form of G_∞. In the compressible case, this is not possible; instead two-point Gaussian quadrature is used over each layer. This leads to the same formal accuracy in (3.1), with the mean error proportional to n_ℓ^{-2}, but in fact Gaussian quadrature proves to be more accurate than explicit integration in the Boussinesq limit (e.g. for ellipsoids, when the exact form of $\boldsymbol{u}$ is known). Evidently, explicit integration over-emphasizes the vertical step-like character of the PV field, while Gaussian quadrature makes it appear smoother. The system evolves through the advection of PV contours,

$$\frac{\mathrm{d}\boldsymbol{x}}{\mathrm{d}t} = \boldsymbol{u}(\boldsymbol{x}, z), \tag{4.1}$$

which is handled numerically by a fourth-order Runge–Kutta method.

The second numerical method, the CASL algorithm (Dritschel & Ambaum 1997), instead computes the velocity field $\boldsymbol{u}$ on a fixed horizontal and vertical grid in a finite domain, here a cylinder (full details are available in Macaskill, Padden & Dritschel 2003). The CASL algorithm solves (2.1*b*) and (2.1*c*) using standard semi-spectral methods (finite difference in radius r and spectral in azimuthal angle θ). The velocity is then interpolated at the contour points in order to use (4.1) for the contour advection. While it is seemingly wasteful to obtain the velocity field everywhere when

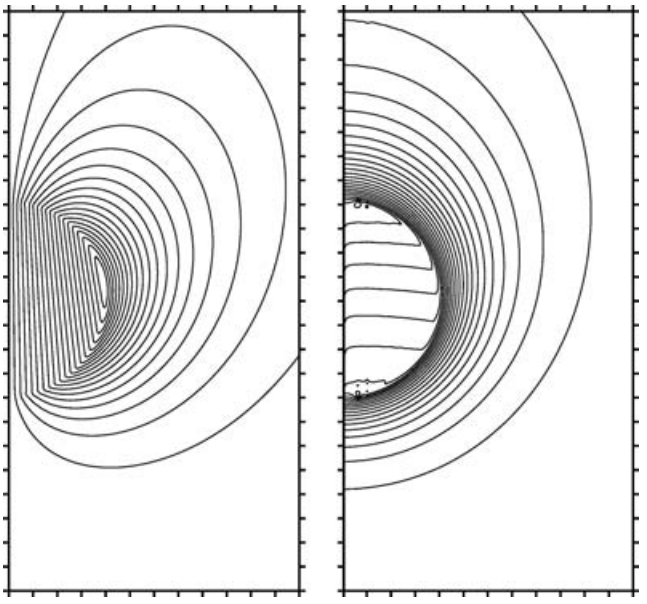

FIGURE 4. As figure 2(*b*) ($D = 2$ case), but computed using the CASL algorithm in a cylindrical domain of total depth $5D$ and radius $5D$. Contour intervals and axes are as in figure 2. Calculation is made using $n_\ell = 512$, $n_r = 512$ and $n_\theta = 1024$.

it is needed only at the contour points, in practice, it is often much more efficient than the explicit contour integration in (3.1). In the results shown here, we use a focused radial grid, spaced uniformly in $r^{1/2}$, to resolve adequately vortices which are small compared to the width of the cylinder. The number of radial and azimuthal grid points, n_r and n_θ, are chosen so that the grid is approximately isotropic at the horizontal edge of the vortices simulated. An example of the flow field computed by CASL is given in figure 4 corresponding to the case $D = 2$ shown in figure 2(*b*) computed by CS. The results are closely similar, despite the finite domain used in CASL. The main differences come from a weaker azimuthal velocity in CASL at the vortex edge, which arises from smearing the PV discontinuity at the vortex edge over one horizontal grid length (Dritschel & Ambaum 1997). For the evolution of the contours however, this has little importance since only the normal velocity component can change the shape of the contours.

The nonlinear simulations presented in § 5.1 and § 5.2 below were carried out using CS to remove completely all boundary effects. We note that the CASL and CS algorithms agree well in all cases, provided a sufficiently large domain is used for the CASL simulations. The bounded simulations presented in § 5.3 were carried out using the CASL algorithm.

5. Nonlinear evolution

Using the numerical methods outlined above, we now consider the nonlinear evolution of some particular ellipsoidal vortices. In the Boussinesq limit these are steadily rotating states, whose various stability properties have been well documented (Meacham 1992; Miyazaki, Ueno & Shimonishi 1999; Dritschel, Scott & Reinaud 2005). In the compressible case considered here, on the other hand, such ellipsoidal vortices are no longer steady states, and so it is not possible to carry out a similarly

detailed stability analysis. However, it is instructive to examine how the compressibility alters the nonlinear evolution in certain cases and how the symmetry of the Boussinesq model is broken.

5.1. *Boussinesq system*

To begin with we recap some stability results of the Boussinesq system and use this system to illustrate a nonlinear wave-activity diagnostic that will prove useful in the examination of the compressible system. We note that the nonlinear dynamics of the instability of freely rotating ellipsoids of the form considered here has not yet been well documented.

We consider ellipsoidal patches of uniform potential vorticity with horizontal aspect ratio $\lambda = a/b$ and vertical aspect ratio $c/\bar{r}$, where $x^2/a^2 + y^2/b^2 + z^2/c^2 = 1$ defines the ellipsoid and where $\bar{r} = \sqrt{ab}$ is the mean horizontal radius. For definiteness we take $a \leqslant b$. For a given $c/\bar{r} \neq 1$, there is a critical horizontal eccentricity λ_c such that for $\lambda_c < \lambda \leqslant 1$ the ellipsoid is stable and for $0 < \lambda < \lambda_c$ it is unstable (Meacham 1992; Dritschel *et al.* 2005). In what follows, we will restrict our attention to prolate vortices with $c/\bar{r} = 4/3$. Note that for $c/\bar{r} = 1$, the ellipsoid is always unstable to a tumbling mode, analogous to that of a solid body rotating about its intermediate inertial axis, but dynamically uninteresting in that the vortex retains its original ellipsoidal shape. Our restriction to prolate vortices is motivated in part by our consideration of atmospheric flows, a particular example where a vortex spans many scale heights being the winter stratospheric polar vortex, for which the value $c/\bar{r} = 4/3$ is not unrealistic. Tests with $c/\bar{r} = 2$ and $c/\bar{r} = 2/3$ indicate that the behaviour described below is robust and only weakly dependent on vertical aspect ratio.

For $c/\bar{r} = 4/3$, the critical value λ_c separating stable and unstable regions is approximately 0.68. We note that this value of λ_c is different from that implied by the analysis of Meacham (1992) and refer the reader to Dritschel *et al.* (2005) for details of why we believe Meacham's M2II mode to be stable.

The nonlinear evolution of the Boussinesq-unstable vortex with $\lambda < \lambda_c$ takes the form of a vertical mode-3 distortion of the vortex. Figure 5 shows the evolution for $\lambda = 0.5$ at selected times before, during and after the instability. Up to about $t = 40$, the vortex retains its original ellipsoidal shape to a good approximation. By $t = 50$, the mode-3 disturbance is well developed, with the central vortex layers extended in one direction and the upper and lower layers extended in the opposite direction. For this λ, well inside the unstable region, the mode-3 deformation is large enough so that weak filamentation occurs in the central layers. However, the largest and most visible filamentation occurs in the upper and lower layers, where the vortex deformation is largest and where substantial material is thrown off symmetrically from the main vortex. The stabilization process can be understood in terms of horizontal ellipticity: during the onset of instability, ellipticity moves towards the vertical extremities, where it is eventually lost to filamentation. In addition, the vertical ellipticity is reduced by the loss of the outermost layers, again to filamentation. The loss of vortex material during filamentation reduces both the horizontal and the vertical aspect ratios, bringing the vortex into a new, stable, quasi-steady configuration. See Dritschel *et al.* (2005) for further discussion of the linear modal structure of the instability and details of the unstable region of parameter space.

The initial elliptical horizontal cross-section can also be regarded as a disturbance to a vortex of circular cross-section, the disturbance having an approximately azimuthal wave-number two structure. The departure from circularity can be regarded as a nonlinear pseudo-momentum-based wave activity, second order in disturbance

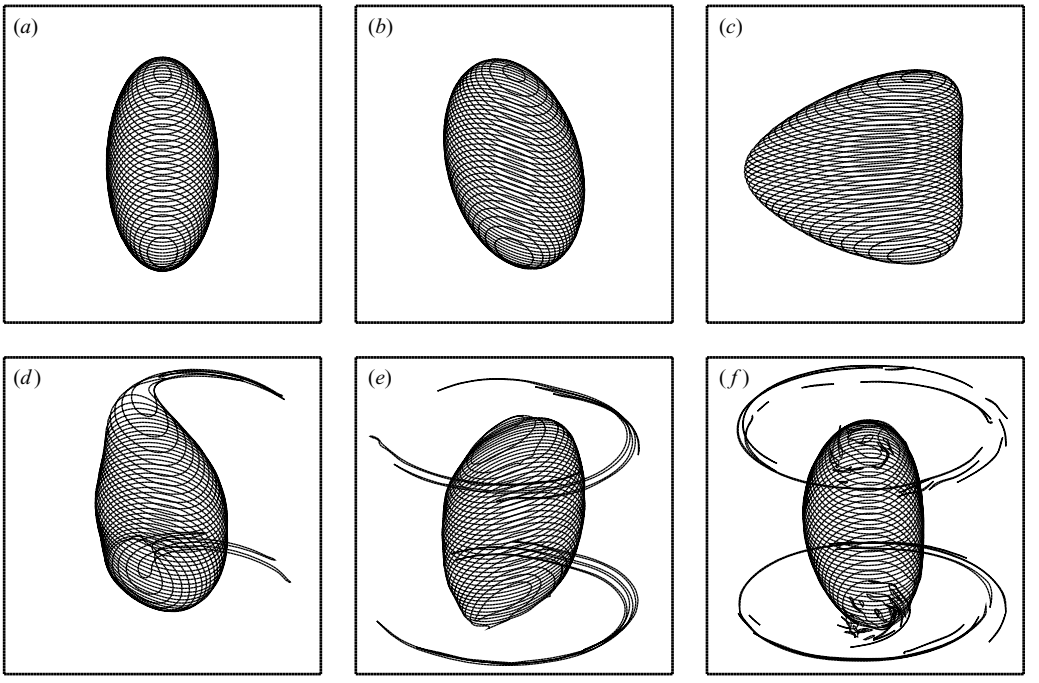

FIGURE 5. Nonlinear evolution of the freely rotating Boussinesq ellipsoid of initial horizontal and vertical aspect ratios $a/b = 0.5$ and $c/\bar{r} = 4/3$, respectively, at times (*a*) $t = 0$, (*b*) 30, (*c*) 50, (*d*) 60, (*e*) 70 and (*f*) 100. Vertical resolution, $n_\ell = 80$. In this and all subsequent images of vortex evolution, only the contours in every second layer are shown.

amplitude, that satisfies an exact conservation relation (Dritschel 1988; Dritschel & Saravanan 1994). The wave activity A can be defined as

$$A(z,t) = \rho(z) q \oint_{\Gamma(z)} [Y(\theta, z, t) - Y_e(z)]^2 \, \mathrm{d}\theta, \tag{5.1}$$

where the integral is taken around a closed contour Γ (or collection of contours, if the original contour breaks up) at height z, θ is an azimuthal coordinate, $Y = r^2/2$ (so that $\mathrm{d}Y\,\mathrm{d}\theta$ is the differential area), $Y_e = r_e^2/2$, and where r_e is the radius of the undisturbed circular contour enclosing the same area as Γ.

Figure 6 shows the evolution of A as a function of height and time. The onset of instability is clearly visible around time $t = 45$. Before that time, the disturbance is initially distributed over the depth of the vortex and remains almost constant in time. Around day 50, the disturbance wave activity propagates rapidly to the upper and lower parts of the vortex at the onset of the instability, where it is eventually dissipated through nonlinear processes. Note that before filamentation begins, the vertical integral of A is exactly conserved. Thus, the rapid increases in A near the vertical extremities around day 50 are exactly balanced by the reduction of A of the central vortex. The instability stabilizes the vortex by moving eccentricity away from the central levels of the vortex and toward the extremities, and eventually removing it through filamentation.

5.2. *Compressible system*

We now look at the nonlinear evolution of the compressible system for vortex configurations having $\lambda < \lambda_c$. For comparison with the Boussinesq case described

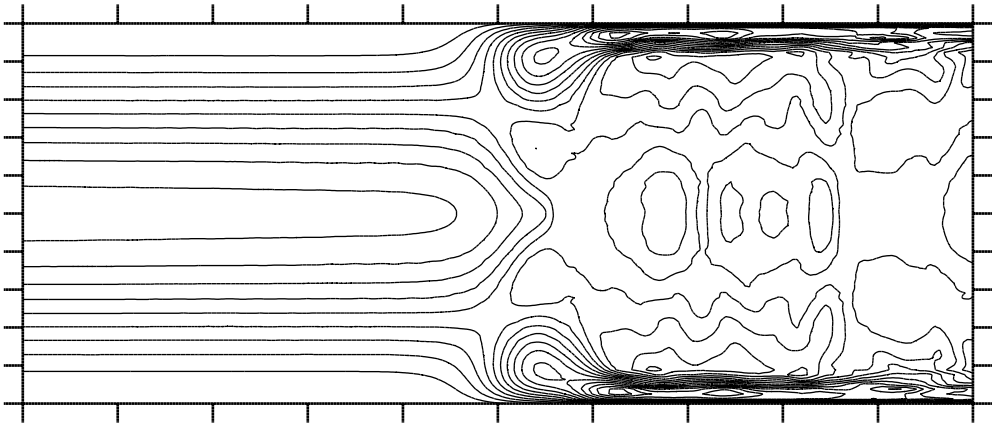

FIGURE 6. Wave activity, A, for the case shown in figure 5 as a function of height within the vortex and time from $t=0$ to $t=100$. Contour interval is 0.0005; tickmarks are every 10 on the horizontal (t) axis and every $D/10$ on the vertical (z)-axis, where D is the (arbitrary) depth of the vortex.

above, we again keep the vertical aspect ratio fixed with $c/\bar{r}=4/3$. Later, we describe briefly the behaviour for other values of $c/\bar{r}$ and for $\lambda > \lambda_c$. Because the compressibility introduces a vertical length scale, $H=1$ in non-dimensional units, we must now consider how the evolution depends on the size of vortex. Since the vertical aspect ratio is fixed, we use the total depth of the vortex, D, as a single parameter to define the vortex size. We expect that for D small compared with H, the evolution should be close to that of the Boussinesq system.

To illustrate the main effect of the compressibility, we begin by presenting the single case $D=2$, for which the nonlinear evolution is shown in figure 7 for times $t=2, 4, 6, 8, 10, 12$. Two features are immediately obvious. First, the vortex deforms rapidly in a much shorter time scale here than in the Boussinesq system, with strong filamentation beginning as early as $t=8$. This should not be completely surprising as the initial configuration is no longer an equilibrium state of the compressible system. Secondly, there is now a strong asymmetry to the evolution, with all deformation occurring in the lower vortex layers. Near the top of the vortex, contours become nearly circular early on in the evolution, whereas near the bottom, they are rapidly elongated and drawn out away from the main vortex. Thus the asymmetry associated with the compressibility has the effect of stabilizing the upper part of the vortex and destabilizing the lower part.

The asymmetry of the evolution can be understood by reference to the asymmetry in the Green's function introduced by the compressibility, and the consequent differential rotation of the upper and lower contours of the vortex. From figure 2(a) we see that for this size of vortex, the Green's function implies a considerable difference between the rotation rates of the upper and lower parts of the vortex. The differential rotation in turn leads to upper and lower vortex contours whose semi-axes either lead or lag, respectively, that of the central vortex. The orientation of these contours to the straining flow induced by the central vortex is depicted schematically in figure 8. Because fluid particles furthest from the axis of rotation (i.e. those at the ends of the longer of the horizontal semi-axes) move slower than those nearest, the dominant straining flow associated with the ellipticity is as represented by the arrows in the figure. The effect of this straining flow on the upper and lower vortex contours is then

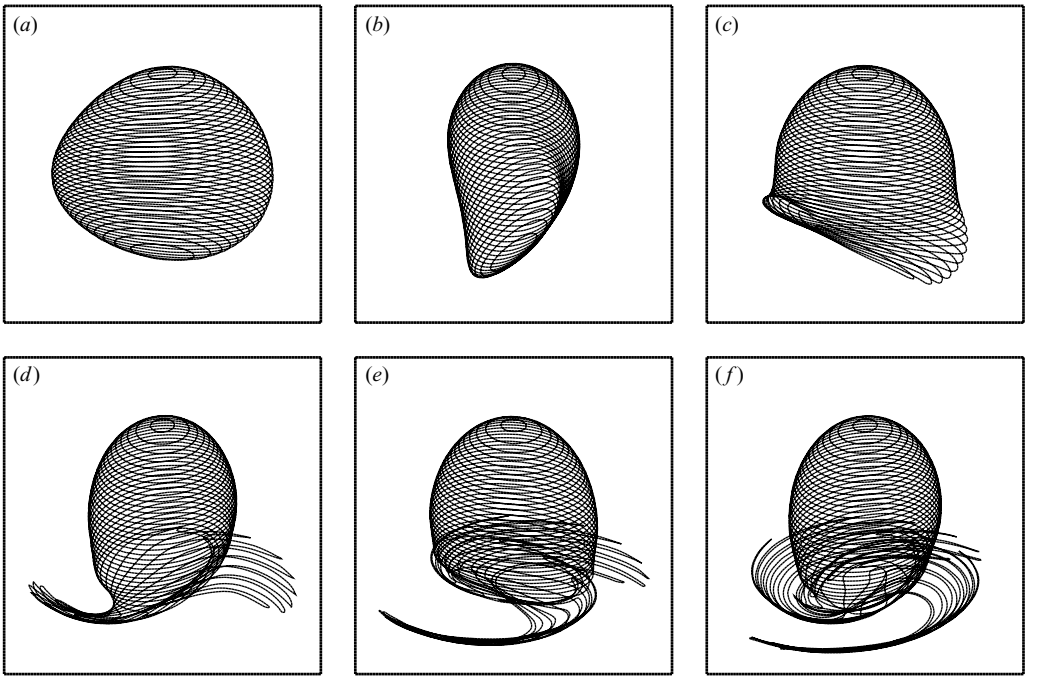

FIGURE 7. Nonlinear evolution for the compressible case of an ellipsoid of initial horizontal and vertical aspect ratios $a/b = 0.5$ and $c/\bar{r} = 4/3$, respectively, and size $D = 2$, at times (*a*) $t = 2$, (*b*) 4, (*c*) 6, (*d*) 8, (*e*) 10, (*f*) 12. Vertical resolution, $n_\ell = 80$.

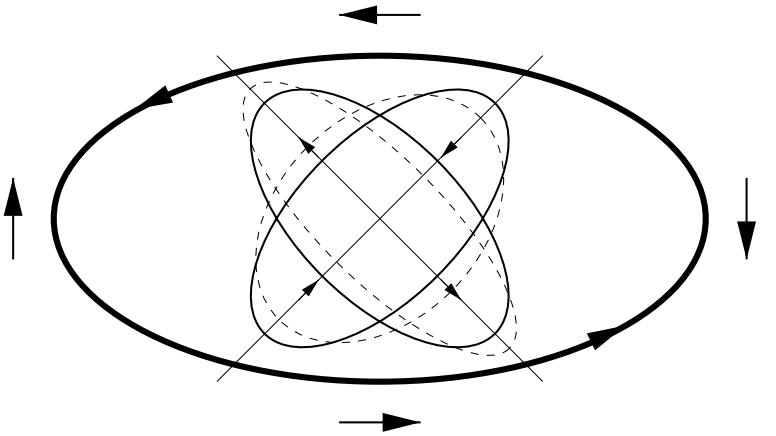

FIGURE 8. Schematic top-view of the effect of the strain induced by the central part of a cyclonic vortex on the upper and lower parts of the vortex, which have faster and slower rotation rates, respectively. A typical contour in the central part of the vortex is denoted by the thick elliptical line with arrows indicating the motion. The straining flow induced by this motion is represented by the large exterior arrows and by the small interior arrows and axes. The thin solid elliptical lines denoted contours near the top and bottom, and the thin dashed lines show those contours at a later time (in a frame of reference rotating with the vortex). The upper contour is squashed toward circularity while the lower contour is elongated.

determined by their orientation. Upper vortex contours rotate faster and align along the compressing axis of the strain flow, and are therefore deformed toward circularity. Lower vortex contours rotate slower and align along the extending axis, and are

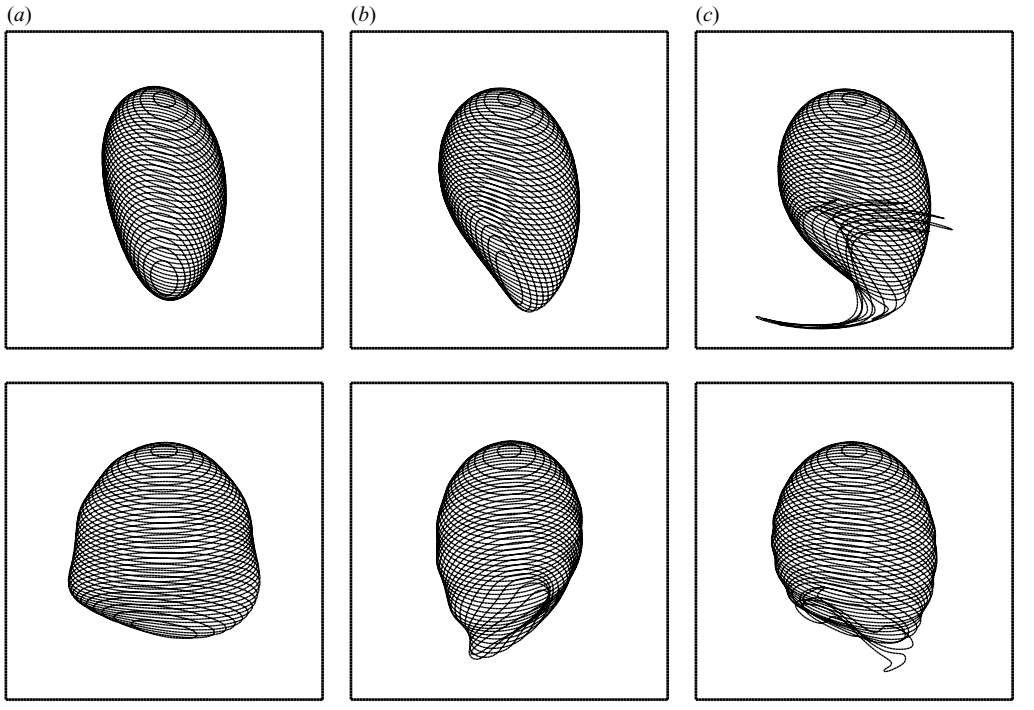

FIGURE 9. As figure 7 but for vortices of size $D = 1/2$ (top panels) and $D = 8$ (bottom panels) at times (*a*) $t = 4$, (*b*) 8, (*c*) 12. Vertical resolution, $n_\ell = 80$.

therefore elongated. The mechanism is analogous to that discussed in Legras & Dritschel (1991) in the context of the inner and outer contours in a distributed two-dimensional vortex. Note that it is completely absent in the Boussinesq case because there the vortex rotation rate is independent of height.

The same behaviour is found over a wide range of vortex sizes. Figure 9 shows the evolution of vortices with $D = 1/2$ (top panels) and $D = 8$ (bottom panels). In both cases the upper vortex contours quickly become circular, while the lower contours elongate and eventually eject material from the vortex. As in the Boussinesq case, the result is a reduction in the average horizontal and vertical aspect ratios of the vortex, and an evolution into new stable quasi-steady state. Note that the effect is largest, i.e. there is greatest vortex deformation and material ejection, when $D \approx 2$, that is for a vortex radius around one density scale height.

The nonlinear evolution described above is somewhat surprising given the mass distribution of the vortex. If wave activity were to propagate equally upward and downward, then particle displacements and filamentation would be expected to be much greater in the upper vortex. Therefore, the behaviour shown in figure 7 suggests that most wave activity propagates downward. Again, this can be understood in terms of the differential rotation of the vortex, together with known properties of Rossby wave propagation: the differential rotation causes the initial elliptic disturbance to tilt with height such that the group velocity is directed downward. Although our results depend on the geometry of our initial ellipsoid and its PV distribution, these considerations also apply to the stratospheric winter polar vortex, which spans a depth of approximately $6H$ and which typically exhibits positive vertical shear throughout that region (see Scott & Dritschel 2005 for more details).

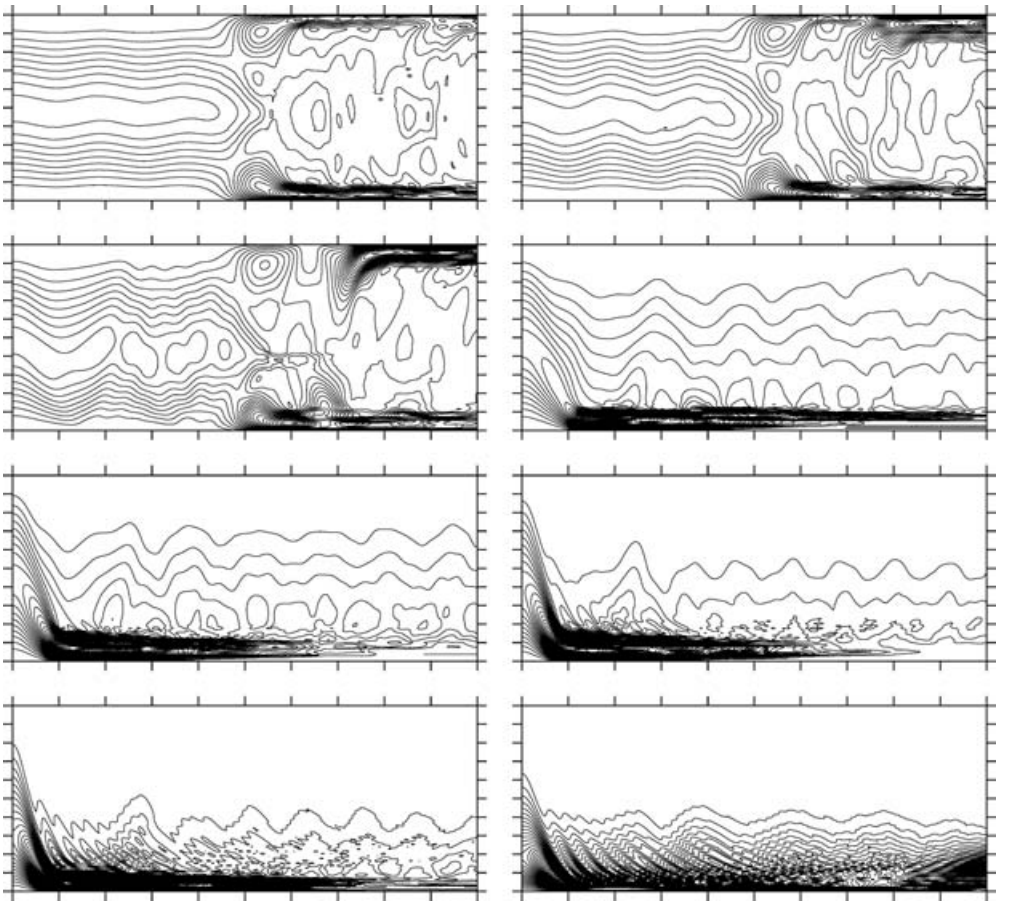

FIGURE 10. Wave activity, A, for the compressible cases and vortex sizes $D = 1/16, 1/8, \ldots, 4, 8$ (left to right and top to bottom) as a function of height within the vortex and time from $t = 0$ to $t = 100$. Contour interval is 0.0005; tickmarks are every 10 on the horizontal (t) axis and every $D/10$ on the vertical (z) axis.

To further illustrate the downward propagation, in figure 10 we plot the wave activity, $A(z, t)$, for a range of vortex sizes $D = 1/16, 1/8, \ldots, 4, 8$. For all cases with $D \geqslant 1/2$, the rapid downward propagation of the initial disturbance is clear. As wave activity is concentrated into the lower levels, its local value increases (again note that the vertical integral is conserved in time in the absence of dissipation) as contours are elongated, before filamentation eventually dissipates wave activity away from the vortex. The vertical asymmetry in A at $t = 0$ results from the density weighting in (5.1).

For $D \leqslant 1/4$, the differential rotation induced by the density asymmetry is no longer large enough to cause a significant downward propagation. In these cases, the Boussinesq mode of instability is dominant, taking the form of an approximately symmetrical vertical mode 3 disturbance (not shown, but similar in character to figure 5). The broken symmetry is still apparent, however, for $D = 1/4$ and $D = 1/8$ in that the lower levels of the vortex exhibit the instability first. Early times of these cases also show an initial downward propagation of wave activity, similar to that seen for larger D, but not strong enough to reach lower levels. Note that the Boussinesq case is recovered in the limit of small D.

Finally, we briefly note the dependence of the nonlinear evolution on the parameters λ and $c/\bar{r}$. The choice $\lambda = 0.5$ was made based on its location well within the unstable mode 3 region of the Boussinesq system, to provide a suitable contrast with the compressible evolution described above. Simulations were also carried out using the larger value of $\lambda = 0.7$, which lies within the stable region of the Boussinesq system. The compressible evolution was qualitatively the same, with downward propagation of wave activity occurring over a large range of vortex sizes, although the magnitude of the wave activity, and the intensity of the lower-level filamentation were reduced, as should be expected.

The vertical aspect ratio of $c/\bar{r} = 4/3$ was chosen so that the Boussinesq mode 3 instability occurred for a moderate value of the horizontal aspect ratio λ. For oblate or more prolate ellipsoids this instability is still present, but for much smaller values of λ. In the compressible case, this value of $c/\bar{r}$ is also appropriate as it is representative of the stratospheric polar vortex, but similar behaviour was observed over a wide range of values. Simulations with $c/\bar{r} = 2$ and $c/\bar{r} = 2/3$, with $\bar{r}$ fixed, showed the same downward propagation of ellipticity and filamentation of the lower vortex layers. In general, the lower vortex filamentation was stronger for more prolate vortices and weaker for oblate vortices, consistent with the stronger density variation across the more prolate vortices.

5.3. *Effect of boundaries*

We now return to the effect of horizontal upper and lower boundaries on the nonlinear evolution. In § 2, we showed how the presence of a lower boundary, in particular, had a significant impact on the structure of the Green's function through the introduction of a barotropic mode which was absent in the vertically unbounded case. It should be expected, therefore, that there will also be a significant change in the nonlinear evolution in the presence of a lower boundary.

We consider a finite vertical domain of depth $12H$ containing an ellipsoidal vortex of horizontal and vertical aspect ratios $\lambda = 0.5$ and $c/\bar{r} = 4/3$, as above, and of vertical extent $6H$, i.e. occupying half the domain depth. The vortex is centred at a height z_0, which is varied between cases to examine the relative influence of the upper and lower boundaries. Here, the CASL algorithm in cylindrical geometry is employed, which is a suitable model for an axisymmetric vortex in a bounded vertical domain (see § 4 above for details and numerical settings). The evolution of five cases is shown in figure 11 for $z_0 = 9, 6, 4.6, 3.6, 3$ (from top to bottom) and at times $t = 4, 12, 40$.

The different types of evolution can be grouped into three categories. For $z_0 > 4$, the evolution is qualitatively similar, each case resembling the evolution of the unbounded case described above, with the disturbance decreasing at upper levels and growing at lower levels until filamentation occurs. Note that this is the case even for $z_0 = 9$ and the vortex is touching the upper boundary; remarkably, the presence of the upper boundary has practically no effect on the evolution.

In contrast, the presence of the lower boundary has a significant effect, and gives rise to a qualitatively different type of evolution. For $z_0 = 3$, i.e. the vortex is touching the lower boundary, the barotropic component of the vortex circulation is significant,

FIGURE 11. Nonlinear evolution for the bounded compressible case, with domain depth $12H$, of an ellipsoid of initial horizontal and vertical aspect ratios $a/b = 0.5$ and $c/\bar{r} = 4/3$, respectively, of vertical extent $D = 6H$, centred at $z_0 = 9, 6, 4.6, 3.6$ and 3 (top to bottom) at times (*a*) $t = 4$, (*b*) 12 and (*c*) 40. Resolution, $n_\ell = 120$, $n_r = 64$, $n_\theta = 128$.

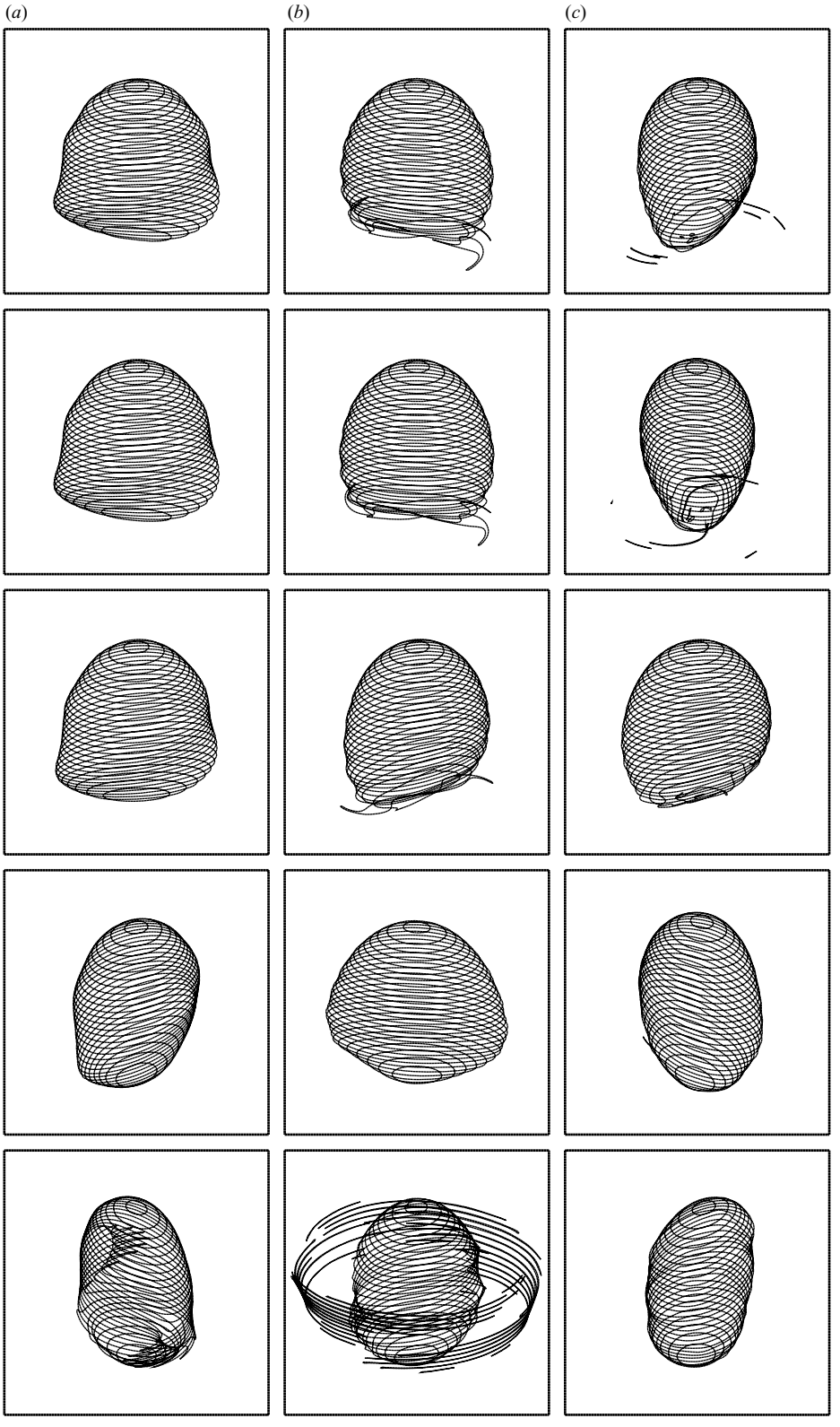

FIGURE 11. For caption see facing page.

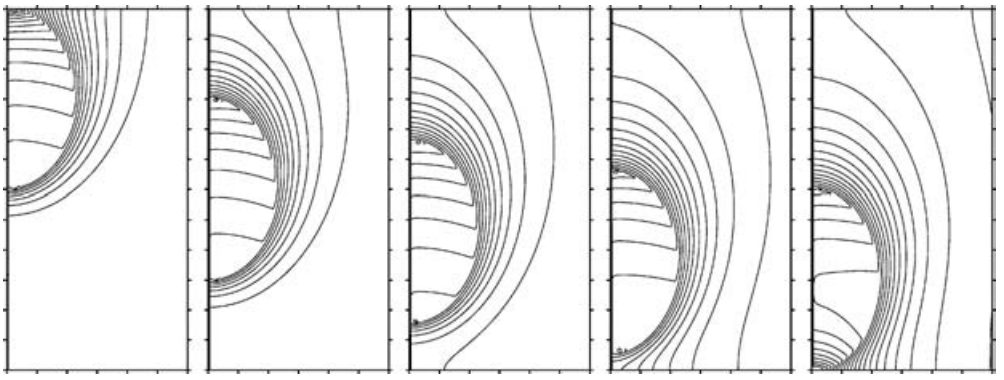

FIGURE 12. Angular velocity corresponding to spheroidal patches of uniform PV (with circular horizontal cross-section) of vertical depth $D = 6H$ in a domain of depth $12H$ and with horizontal radius $\bar{r} = 2.25$, centred at heights (from left to right) $z_0 = 9$, 6, 4.6, 3.6, 3. Contour interval is 0.2; tickmarks on horizontal (r) and vertical (z) axes are every horizontal length scale L and vertical scale height H, respectively. Resolution, $n_\ell = 256$, $n_r = 384$, $n_\theta = 768$.

in accordance with the structure of the bounded Green's function shown in figure 1. As a consequence, the vortex experiences a much stronger barotropic straining flow, which results in the rapid filamentation of the vortex. Further, because the straining field is strongest at a radius approximately equal to the average vortex radius, the central levels experience a stronger strain than the upper and lower extremities, and filamentation occurs first at these central levels.

The difference in behaviour can again be best understood in terms of the differential rotation. Figure 12 shows the angular velocity associated with a spheroid of the same vertical aspect ratio ($c/\bar{r} = 4/3$) at the corresponding heights in the domain ($z_0 = 9$, 6, 4.6, 3.6, 3 from left to right). For $z_0 = 9$, the effect of the upper boundary is to intensify the rotation of the uppermost vortex, increasing the differential rotation and stabilizing the vortex. Because the rotation of the lower vortex is unaffected by the upper boundary, the nonlinear evolution is also largely unaffected. On the other hand, for $z_0 = 3$, the effect of the lower boundary is to reverse the sense of the differential rotation, stabilizing the lower most vortex, but rendering the mid-levels unstable to the same mechanism as that described in figure 8. There is thus change in the topology of the rotation as the distance between the vortex and the lower boundary is reduced.

Between these two extremes lies a third type of evolution. For $z_0 = 3.6$, we find the surprising result that no instability occurs. At this distance from the boundary, it appears that there is an almost exact cancellation in the lower vortex between the differential rotation induced by the compressibility and the reversal associated with the lower boundary. Thus, it appears that for $z_0 = 3.6$, the whole lower vortex rotates quasi-rigidly, and the deformation mechanism described in figure 8 is absent.

Finally, we show in figure 13 the wave activity for the five cases described above. In each of the three cases with $z_0 > 4$, the downward propagation of wave activity is clear. Note that there is an initial strong downward pulse followed by repeated and progressively weaker and slower pulses as the reservoir of wave activity in the vortex is depleted. Evidence of this downward propagation is clear as far out as $t = 50$, long after the initial pulse has cause the destruction of the lower vortex, and indicates the robustness of this feature.

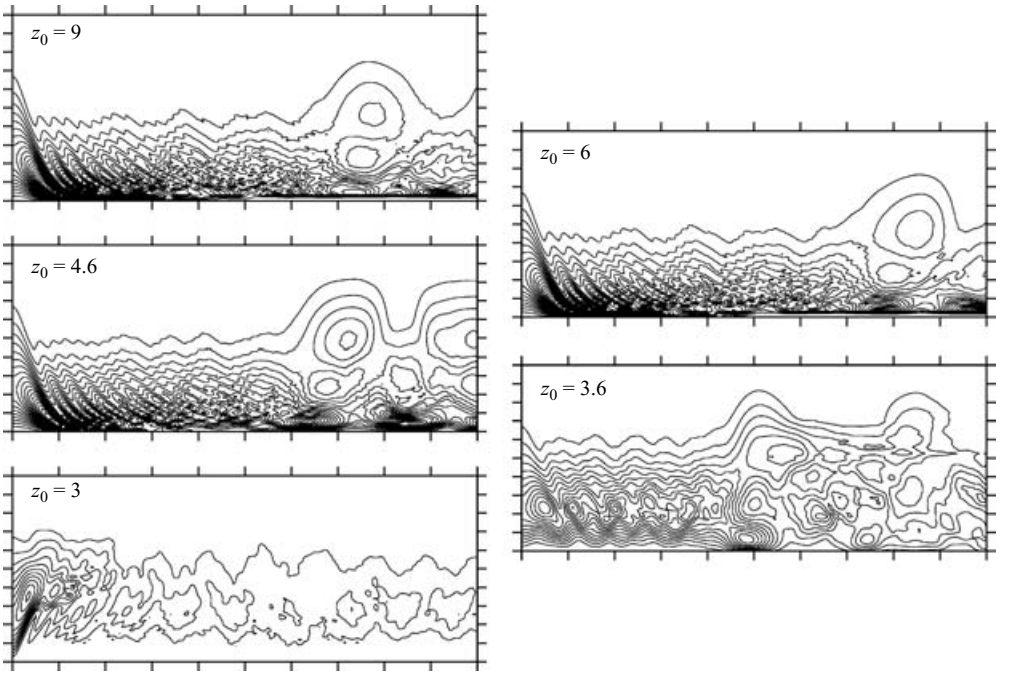

FIGURE 13. Wave activity, A, for the bounded compressible cases shown in figure 11 as a function of height within the vortex and time from $t = 0$ to $t = 100$. Contour interval is 0.001; tickmarks are every 10 on the horizontal (t) axis and every scale height H on the vertical (z) axis.

For $z_0 = 3$, on the other hand, the dominant effect of the lower boundary is clear: wave activity remains concentrated near the central levels of the vortex as these are rapidly distorted. There is even some evidence of upward propagation over the first few days of the simulation. By day twenty, the intense filamentation seen in figure 11 has led to the depletion of almost all of the original wave activity of the vortex.

In the intermediate regime with $z_0 = 3.6$, there is a hint of downward propagation, but the maximum in wave activity remains around 2–3 scale-heights above the lower boundary. Because there is no filamentation in this case, the domain average wave activity remains constant throughout the simulation, with only small local changes caused by gentle undulations of the unsteady vortex.

6. Discussion

We have shown how certain dynamical features of the compressible quasi-geostrophic system can be understood naturally in terms of a simple expression for the Green's function, which makes explicit the dependence of PV inversion on spatial direction. In contrast to the three-dimensional Boussinesq system, the Green's function in the compressible system, in which density decreases exponentially with height, has an exponential decay in all directions except vertically upward, in which case the decay is like $1/R$. The anisotropic dependence is a direct consequence of the anisotropy of the background density profile, and vanishes in the Boussinesq limit.

The anisotropy of the Green's function has important consequences for the nonlinear evolution of a finite volume PV anomaly. In particular, because the induced circulation is stronger above than below, the upper parts of a coherent vortex will

in general rotate faster than the lower parts. This was demonstrated explicitly for a spherical PV patch, but is also valid for more general PV distributions.

The consequences of this differential rotation on perturbed vortices are particularly startling when the half-depth of the vortex is of the same order as the vertical density scale height. For vortices with a horizontal elliptical disturbance, the effect of the differential rotation combines with the straining flow associated with the ellipticity to ensure that ellipticity is reduced in the upper vortex and enhanced in the lower vortex, giving rise to a purely downward propagation of the disturbance. Given that the density decreases exponentially with height, this result is somewhat counter intuitive: particle excursions associated with a given amount of wave activity being larger where the density is lower, one would expect contour displacements to grow exponentially with height. However, as seen in the simulations of § 5.2, wave activity in the upper vortex decreases rapidly as the upper vortex is stabilized by the straining flow and the differential rotation, and grows rapidly in the lower vortex. For the parameters chosen above, the effect is strongest, as measured by the destruction of the lower vortex, when the half-depth of the vortex is exactly one density scale height.

Although we presented simulations of purely ellipsoidal vortices, we believe the above mechanism to be robust and present in a wider range of situations. Consider, for example, the wave activity shown in the last panel of figure 10 in which $D = 8$, approximately representative of the stratospheric polar vortex. In addition to the initial downward propagation event prior to $t = 10$, there are numerous subsequent events long after the vortex has lost its initially ellipsoidal shape. In light of recent interest in the ability of dynamical events in the stratosphere to influence tropospheric weather patterns (e.g. Baldwin & Dunkerton 2001) an interesting question is whether such a mechanism for downward propagation is at play in the atmosphere.

The introduction of horizontal lower and upper boundaries into the system leads to further unexpected properties, which can again be understood in terms of the Green's function in a bounded domain. Remarkably, an upper boundary has almost no effect on the structure of the Green's function, nor, because it is stabilizing, on the nonlinear evolution of finite vortices. In contrast, the presence of a lower boundary close to the source point changes the structure of the Green's function significantly through the introduction of a large barotropic component. The change occurs when the lower boundary is within around a density scale height from the source point.

The effect of a lower boundary on the nonlinear evolution of a finite vortex is similarly dramatic. When the vortex is close to the boundary, the increase of the Green's function response owing to the boundary acts to reverse the differential rotation in the lower vortex, with the result that the lowermost vortex is stabilized and the entire mid-level vortex is strongly deformed. A surprising regime is found for a critical separation between the vortex and the lower boundary, where the reversal induced by the boundary is too weak to destabilize the mid-level vortex, but strong enough to cancel the differential rotation in the lower vortex associated with the anisotropy of the unbounded Green's function. In this regime, the vortex remains coherent for a remarkably long time, with no growth of disturbances or filamentation. Since the critical separation corresponds closely (in terms of density scale heights) to the separation between the stratospheric polar vortex and the ground, an investigation of the effect of the lower boundary on the inversion of more realistic atmospheric PV distributions seems warranted.

Finally, we note that, unlike in the Boussinesq system, the ellipsoidal initial conditions used in the nonlinear simulations of the compressible system above are not exact steadily rotating solutions of the governing equations. Given the explicit

form of the Green's function, however, it is now possible to use the techniques described in Reinaud & Dritschel (2002) to search for equilibria of single vortices in the compressible system. Finding these would permit a more detailed and systematic analysis of the stability of ellipsoidal vortices in a wider range of parameter space.

We thank Peter Haynes for helpful comments on the manuscript and for drawing our attention to the analogous Green's function of the advection–diffusion operator. Support for this research was provided by the UK Natural Environment Research Council under grant number NER/B/S/2002/00567.

REFERENCES

Baldwin, M. P. & Dunkerton, T. J. 2001 Stratospheric harbingers of anomalous weather regimes. *Science* **294**, 581–584.

Dritschel, D. G. 1988 Nonlinear stability bounds for inviscid, two-dimensional, parallel or circular flows with monotonic vorticity, and the analogous three-dimensional quasi-geostrophic flows. *J. Fluid Mech.* **191**, 575–582.

Dritschel, D. G. 1989 Contour dynamics and contour surgery: numerical algorithms for extended, high-resolution modelling of vortex dynamics in two-dimensional, inviscid, incompressible flows. *Comput. Phys. Rep.* **10**, 78–146.

Dritschel, D. G. 2002 Vortex merger in rotating stratified flows. *J. Fluid Mech.* **455**, 83–101.

Dritschel, D. G. & Ambaum, M. H. P. 1997 A contour-advective semi-Lagrangian numerical algorithm for simulating fine-scale conservative dynamical fields. *Q. J. R. Met. Soc.* **123**, 1097–1130.

Dritschel, D. G. & Saravanan, R. 1994 Three-dimensional quasi-geostrophic contour dynamics, with an application to stratospheric vortex dynamics. *Q. J. R. Met. Soc.* **120**, 1267–1297.

Dritschel, D. G., Scott, R. K. & Reinaud, J. N. 2005 The stability of quasi-geostrophic ellipsoidal vortices. *J. Fluid Mech.* (In press).

Legras, B. & Dritschel, D. G. 1991 The elliptical model of two-dimensional vortex dynamics. Part I: The basic state. *Phys. Fluids* **A 3**, 845–854.

Macaskill, C., Padden, W. E. P. & Dritschel, D. G. 2003 The CASL algorithm for quasi-geostrophic flow in a cylinder. *J. Comput. Phys.* **188**, 232–251.

Meacham, S. P. 1992 Quasigeostrophic, ellispoidal vortices in a stratified fluid. *Dyn. Atmos. Oceans* **16**, 189–223.

Miyazaki, T., Ueno, K. & Shimonishi, T. 1999 Quasigeostrophic, tilted spheroidal vortices. *J. Phys. Soc. Japan* **68**, 2592–2601.

Morton, K. W. 1996 *Numerical Solution of Convection–Diffusion Problems.* Chapman & Hall.

Pedlosky, J. 1987 *Geophysical Fluid Dynamics.* Springer.

Reinaud, J. N. & Dritschel, D. G. 2002 The merger of vertically offset quasi-geostrophic vortices. *J. Fluid Mech.* **469**, 287–315.

Scott, R. K. & Dritschel, D. G. 2005 Downward wave propagation on the polar vortex. *J. Atmos. Sci.* (In press).

Waugh, D. W. & Dritschel, D. G. 1991 The stability of filamentary vorticity in two-dimensional geophysical vortex-dynamics models. *J. Fluid Mech.* **231**, 575–598.

Waugh, D. W. & Dritschel, D. G. 1999 The dependence of Rossby wave breaking on the vertical structure of the polar vortex. *J. Atmos. Sci.* **56**, 2359–2375.